

*This article has been submitted for review in the Journal of Geophysical Research  
- Machine Learning and Computation.*

## **Leveraging power of deep learning for fast and efficient elite pixel selection in time series SAR interferometry**

Ashutosh Tiwari\*, Nitheshnirmal Sadhashivam, Leonard O. Ohenhen and Manoochehr Shirzaei

Department of Geosciences, Virginia Tech, Blacksburg, VA, USA

Virginia Tech National Security Institute, Blacksburg, VA, USA

Corresponding author: Ashutosh Tiwari ([ashutoshtiwari796@gmail.com](mailto:ashutoshtiwari796@gmail.com), [ashutosh22@vt.edu](mailto:ashutosh22@vt.edu))

### **Key Points:**

- An improved deep learning model for selection of elite pixels in time series InSAR.
- Different models developed for urban and coastal sites.
- Models fastest in performing pixel selection compared to traditional InSAR processors, without compromising on quality of selected pixels.

## Abstract

This work proposes an improved convolutional long short-term memory (ConvLSTM) based architecture for selection of elite pixels (i.e., less noisy) in time series interferometric synthetic aperture radar (TS-InSAR). Compared to previous version, the model can process InSAR stacks of variable time steps and select both persistent (PS) and distributed scatterers (DS). We trained the model on ~20,000 training images (interferograms), each of size  $100 \times 100$  pixels, extracted from InSAR time series interferograms containing both artificial features (buildings and infrastructure) and objects of natural environment (vegetation, forests, barren or agricultural land, water bodies). Based on such categorization, we developed two deep learning models, primarily focusing on urban and coastal sites. Training labels were generated from elite pixel selection outputs generated from the wavelet-based InSAR (WabInSAR) software developed by Shirzaei (2013) and improved in Lee and Shirzaei (2023). With 4 urban and 7 coastal sites used for training and validation, the predicted elite pixel selection maps reveal that the proposed models efficiently learn from WabInSAR-generated labels, reaching a validation accuracy of 94%. The models accurately discard pixels affected by geometric and temporal decorrelation while selecting pixels corresponding to urban objects and those with stable phase history unaffected by temporal and geometric decorrelation. The density of pixels in urban areas is comparable to and higher for coastal areas compared to WabInSAR outputs. With significantly reduced time computation (order of minutes) and improved selection of elite pixels, the proposed models can efficiently process long InSAR time series stacks and generate rapid deformation maps.

**Keywords:** Time series InSAR, convolutional long short term memory networks, measurement pixel selection

## Plain Language Summary

This study proposes an improved deep learning based model for selecting elite (less-noisy) pixels in time series interferometric synthetic aperture radar (TS-InSAR). We train using urban and coastal areas separately, developing two different models, capable of detecting elite pixels in urban and non-urban terrain. The pixel selection step consumes significant amount of time in TS-InSAR processing chain, and the proposed models perform pixel selection in order of a few minutes, with comparable accuracy.

## 1. Introduction

Time series interferometric synthetic aperture radar (TS-InSAR) has been used extensively over the last decade to monitor natural and anthropogenic surface deformation owing to its high density of observations with reliable phase change information. With a further rise in the datasets thanks to the present (Sentinel-1, RADARSAT, ALOS PALSAR, TerraSAR-X) and upcoming (NISAR, Tandem-L, COSMO-SkyMed second generation, TerraSAR-3) SAR data missions [Galvani *et al.*, 2016; Hajnsek *et al.*, 2014; Kellogg *et al.*, 2020; Mari *et al.*, 2018; Moreira *et al.*, 2011; Rosen

and Kumar, 2021; Rosenqvist et al., 2023], the processing requirements are and going to be more demanding. It is, hence, incumbent upon researchers, scientists, and engineers working on InSAR to devise efficient ways of data processing, transfer, and storage using advanced data structures, memory management, and information mining techniques. The overall TS-InSAR processing chain generally involves preprocessing the single look complex (SLC) SAR images (for orbit determination, multi-looking, burst removal for Sentinel-1) followed by co-registration, interferogram generation and partial topographic phase removal through an external digital elevation model [Ferretti et al., 2011; Hanssen, 2001; Hooper, 2008; Hooper et al., 2007; Lee and Shirzaei, 2023; Shirzaei, 2012]. These steps yield a stack of differential interferograms ready for time series processing. Different methods are used to perform TS-INSAR, mostly chosen based on the phenomena investigated and the terrain characteristics (Agram et al., 2013; Ferretti et al., 2011; Hooper, 2008; Hooper et al., 2007; Shirzaei, 2012). The methods perform the selection of elite (less-noisy) pixels, phase unwrapping, estimation and removal of nuisance phase, and displacement estimation to evaluate the spatiotemporal deformation pattern. The pixel selection step here is critical in governing the observation set for the succeeding steps. The density and quality of pixels vary due to different types of terrain, object characteristics (artificial or natural), geometrical and temporal decorrelation, and deformation behavior. Two types of scatterers are useful for interferometry, (i) persistent scatterers (PS) and (ii) distributed scatterers (DS), and we categorize these as elite pixels for this study too [Agram et al., 2013; Ferretti et al., 2011].

With the requirement of spatio-temporal analysis of millions of pixels present in a differential interferogram stack, elite pixel selection consumes a significant chunk of processing time for most TS-InSAR processors [Jiang et al., 2014; Reza et al., 2017]. For methods working only with PS pixels, the quality and density of elite pixels also suffer in the case of non-urban areas, where PS pixels are rare [Chen et al., 2023; Wang et al., 2022; Zhang et al., 2022]. Moreover, the conventional methods used by most of these processors cannot reduce the processing time, typically taking hours and sometimes days in case the computational resources are constrained. We see that artificial intelligence tools are proving invaluable for various fields of research including earth observation studies, providing methods that are computationally efficient and accurate. For InSAR studies too, we see research related to volcano detection [Anantrasirichai et al., 2019a], urban area deformation analysis [Anantrasirichai et al., 2019b], land subsidence [Radman et al., 2021], landslide zones and slope instability [Devara et al., 2021; Yuan and Chen, 2022], measurement pixel selection [Lattari et al., 2022; Tiwari et al., 2020], phase unwrapping [Sica et al., 2020; Zhou et al., 2022], deformation prediction [Rouet-Leduc et al., 2021] and post-processing deformation signals [Festa et al., 2023; Rygus et al., 2023; Tiwari and Shirzaei, 2024].

Motivated by the challenges present in elite pixel selection and the promising outcomes from AI-related methods, we propose a deep learning-based approach to perform elite pixel selection in the TS-InSAR processing chain for this study. This study aims to develop deep learning architectures automating the selection of elite (both PS and DS) pixels in TS-INSAR with reduced

computational requirements and comparable or better selection quality. We build a model named convolutional long short term memory network for interferometric semantic segmentation (CLSTM-ISS) version 2, an improvement over the model proposed in [Tiwari *et al.*, 2020]. The model has been improved to accommodate any and flexible number of interferometric time series images, since the earlier model could work with a fixed (10) number of time steps. The other improvement is over selecting both PS and DS pixels, as the earlier model worked for PS selection alone. Another modification is the decision to develop multiple deep learning models, each suited to a particular type of terrain rather than one generalized model satisfying all study sites. It may be debatable that one generalized model can be built and replaced with multiple specific models for pixel selection. We however believe that for the problem statement addressed here, the cost of misinterpretation of deformation pattern and the reliability of reported deformation estimates is more significant than having an ease of using a single generalized model.

The paper is organized as follows. Section 2 details the dataset preparation for training the deep learning models. Section 3 describes the proposed CLSTM-ISS v2.0 architecture. Section 4 presents the results obtained and discussions, followed by conclusions in section 5.

## 2. Study sites and datasets

Based on the diversity of the acquisition geometry, terrain characteristics, deformation behavior, and user interests, we focus this study on two different types of study sites, urban and coastal. To cover the whole spectrum of scatterers, we chose some of the coastal sites encompassing non-urban features like hills, barren areas, forests, and water bodies. We seek to build separate deep learning models for urban and coastal sites characterized by different geometric effects (foreshortening, layover and shadow), land use/land cover characteristics (forest, urban, agricultural, barren land, etc.) affected by varied deformation types (linear or non-linear) and phenomena (land subsidence, uplift, landslides, earthquakes, volcanic activity, etc.). Figure 1C shows a schematic view of the object backscatter responses received for different types of terrain. Figure 1(D) shows that urban areas and man-made infrastructure receive responses like that of PS, while agricultural fields give a DS-like response. Coastal sites also have a human population with a few man-made structures and natural objects, yielding both PS- and DS-like responses. Forest areas generally contain poor scatterers, and hilly areas retain PS in case of foreshortening, which results in noisy scatterers for layover and shadowing affected areas. We use four urban and six coastal sites for training and two sites each for testing the urban and coastal models. Figures 1A and 1B show the urban and coastal sites, respectively. The first type of model, named the ‘urban model,’ uses four cities in the United States for training, spread well apart having different distribution of buildings and infrastructure, and having different deformation behavior altogether, as evident from [Castellazzi *et al.*, 2016; Parsons *et al.*, 2023; Qiao *et al.*, 2023a; Qiao *et al.*, 2023b; Qu *et al.*, 2023; Wu *et al.*, 2022]. We chose the United States East Coast to train the second

model type and named it the ‘coastal model’ for simplicity here. The East coast with ~3500 km coastline, has varying terrain characteristics containing forests and agricultural lands, and a few settlements inland, and is affected by land subsidence [Ohenhen *et al.*, 2024; Ohenhen *et al.*, 2023; Sherpa *et al.*, 2023; Xi *et al.*, 2023; Yin, 2023]. More information on the dataset parameters are provided in Supplementary Tables 1.1 and 1.2.

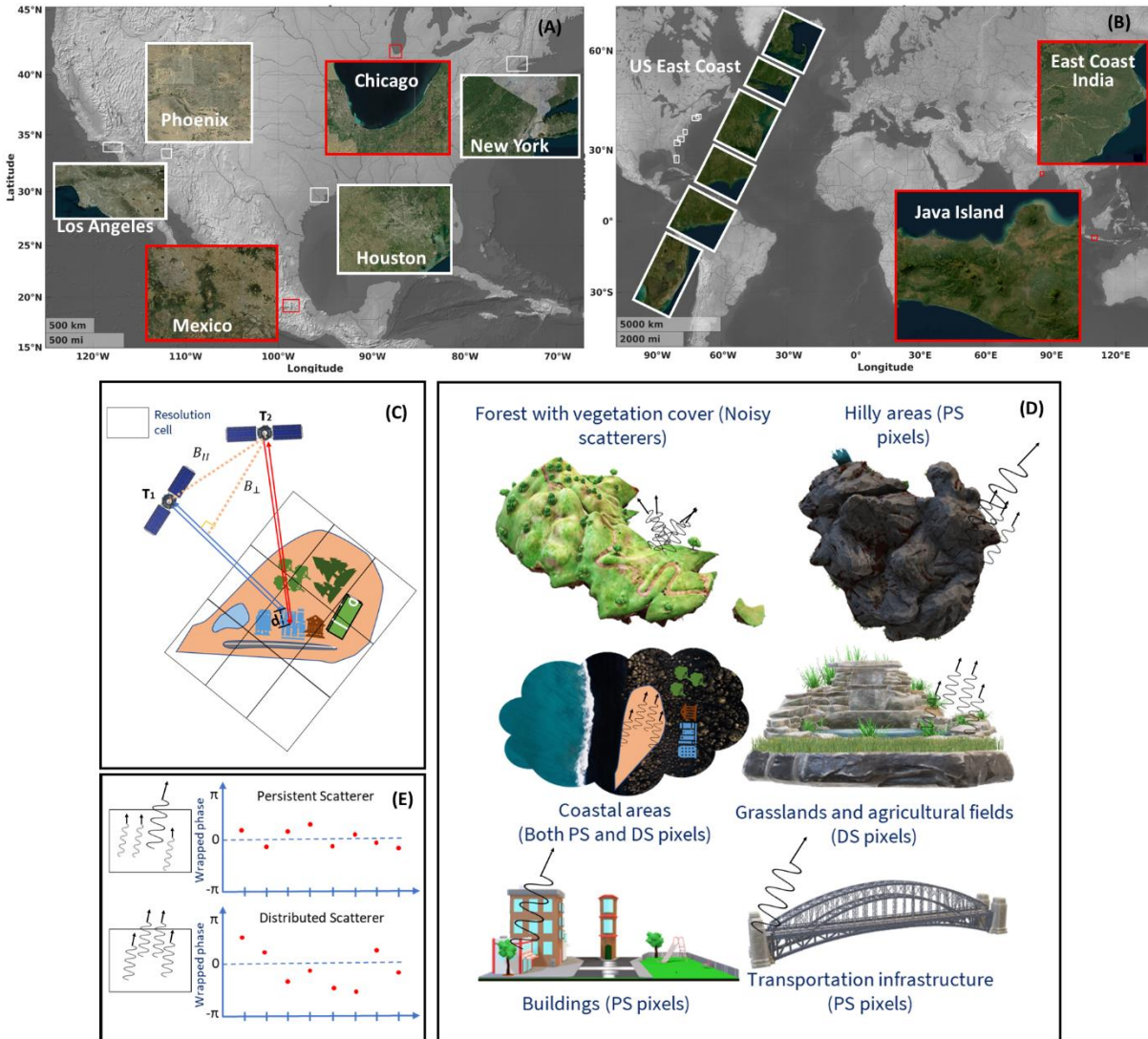


**Figure 1:** A schematic view of target responses in SAR interferometry. (A) and (B) show study sites used for training the urban and coastal sites, respectively. White and red border rectangles denote training and test datasets, respectively. (C) and (D) show InSAR geometry and the scattering response mechanisms for different terrains. (E) shows a sample temporal response from persistent and distributed scatterers.

We divide each differential interferogram into patches of 100 by 100 pixels, making them suitable for memory management during the training of the deep learning models and also increasing the sample size. This results in ~20,000 images used for training. We use labels of elite (persistent and distributed) pixels extracted from the Wavelet-based InSAR (WabInSAR) processing chain proposed in Shirzaei (2013), and improved in Lee and Shirzaei (2023). WabInSAR method uses a statistical approach to perform elite pixel selection, initially selecting PS candidates based on a specified threshold on amplitude dispersion index  $D_A$ , as shown in equation 1.1, where  $\sigma_a$  and  $\mu_a$  denote the standard deviation and mean values of pixel amplitude for the time series. Later, DS candidates are selected using the coherence dispersion threshold  $D_c$  as shown in equation 1.2, where  $\sigma_c$  and  $\mu_c$  represent the standard deviation and mean of the pixel coherence values for the time series. The DS candidates go under statistical evaluation with the PS pixels. We form voronoi cells containing PS candidates and identify their neighboring DS candidates, the cell size is decided based on the density of PS pixels. The DS candidates that satisfy statistical similarity with a PS candidate in a cell based on the Fisher's test of distribution similarity (equation 2) are considered elite pixels and are retained along with PS candidates to act as the final set of elite pixels. In equation 2,  $F$  stands for the  $F$ -statistic value from the Fisher's distribution,  $\sigma_{PS}$  stands for the amplitude standard deviation of the PS pixel over time, and  $\sigma_{DS}^j$  stands for the standard deviation of the  $j^{\text{th}}$  DS candidate pixel within the Voronoi diagram. If the computed value of  $F$  turns out to be greater than the theoretical value, the pixel is included as an elite pixel and rejected otherwise. More details on this approach can be seen in Lee and Shirzaei (2023).

$$D_A = \frac{\sigma_a}{\mu_a} \approx \sigma_{\phi_{noise}} \tag{1.1}$$

$$D_c = \frac{\sigma_c}{\mu_c} \tag{1.2}$$

$$F = \frac{(\sigma_{DS}^j)}{(\sigma_{PS})}, j=1..q \tag{2}$$

We divide the training set into a training and validation ratio of 70:30 for each training site. Most datasets we use in training contain about 80 to 150 time steps. However, for many research labs, it is challenging to process interferometric stacks with 100 time steps due to constrained computational resources compared to the humongous processing size requirements. To this end, we resample each interferometric stack to 25-30 time steps, with the model capable of accommodating stacks with different time steps.

### 3. Proposed deep learning architecture

The proposed architecture is shown in Figure 2. Prior to learning, we saw that the interferograms were divided into patches, each with a size of 100 by 100 pixels. Subsequently, the time series are sampled to fewer time steps (25 to 30). The dimension of input passed to the architecture is  $(n_s, n_t, w, h, f)$  where  $n_s$  and  $n_t$  represent the number of image samples and time steps respectively,  $w$  and  $h$  denote the image width and height respectively (100 each in this study), and  $f$  denotes the number of features used for learning. The model consists of an input layer, two hidden convolutional LSTM layers named *convlstm*, a convolutional layer *conv* dedicated to spatial learning once the time series features are identified, and an output layer. To combat overfitting, the model encompasses a normalization layer between *convlstm*<sub>1</sub> and *convlstm*<sub>2</sub>, a batch normalization layer between *convlstm*<sub>2</sub> and *conv*, and a dropout layer between *conv* and the last fully connected *FC* layers.

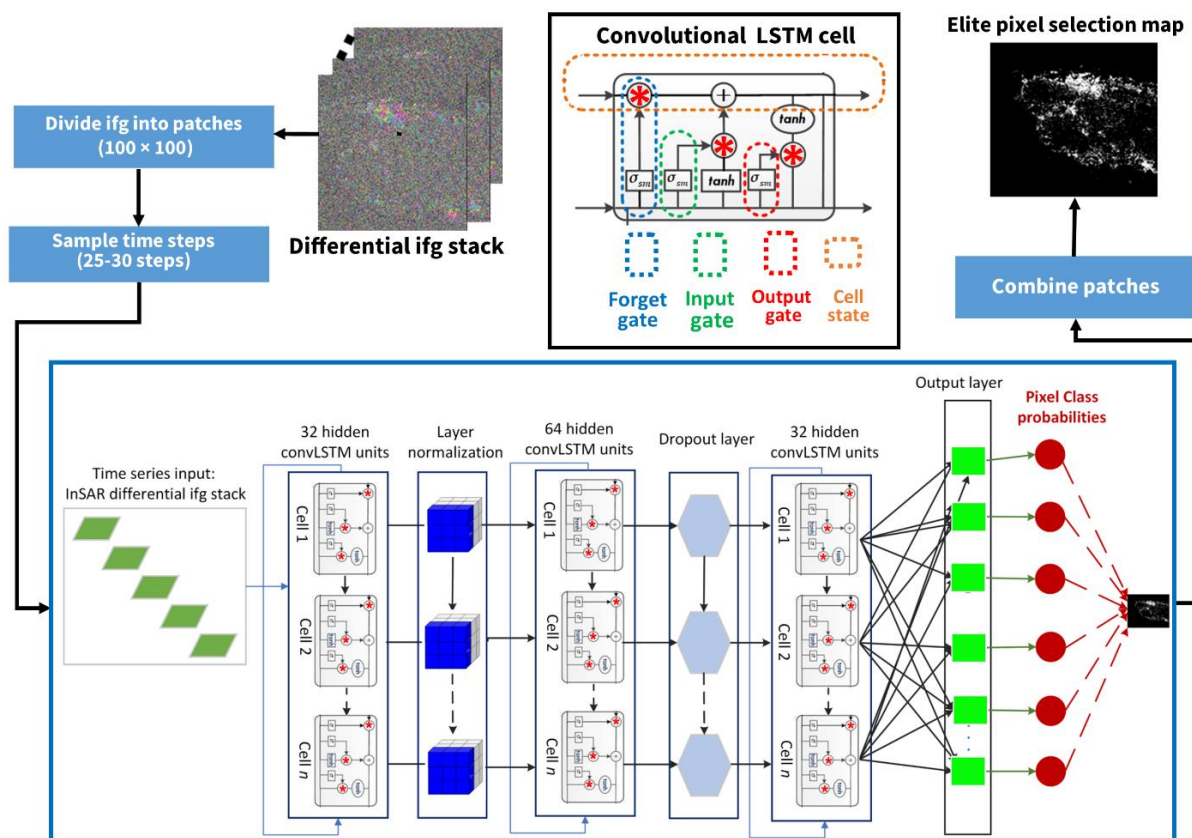


Figure 2: Proposed method for elite pixel selection. Interferograms are divided into small patches of size 100 by 100 pixels and sampled in fewer time steps (25-30). This goes to the CLSTM-ISS v2.0 model for learning. Later, the output patches are combined to create the full elite pixel selection map for the input interferogram stack.

The structure of a *convlstm* cell is also shown in Figure 2. Like an LSTM cell, it has three gates; forget, input and output, and a cell state. The operations of the cell state and the gates are similar, except for the fact that the convolution operation replaces each scalar multiplication present in an LSTM cell. This enables the *convlstm* layer spatially within a specified neighborhood (size of convolution kernel), and temporally with the basic LSTM structure. Equations 3.1 to 3.5 give the mathematical explanations of the three gates and the cell state. The response from the forget, input, and output gates obtained for time step  $t$  are represented as  $fg_t$ ,  $in_t$  and  $out_t$  respectively. All these gates work with the output received from the previous time step  $y_{t-1}$  and the input at the current time step  $x_t$ . A sigmoid activation is applied to the output of the three gates, with weights and biases different for each gate, denoted as  $(w_{fg}, b_{fg})$ ,  $(w_{in}, b_{in})$  and  $(w_{out}, b_{out})$  for the forget, input, and output gates respectively. Learning over iterations, the forget gate determines and discards unwanted information from the time series (equation 3.1). Similarly, the input gate estimates and retains the useful information in the time series (equation 3.2). The cell uses the output of the forget and input gates to compute a predicted cell state. The final cell state is computed by adding the outputs received from convolving the present forget gate response  $fg_t$  with the previous time step cell state  $S_{t-1}$ , and by convolving the present input gate response  $in_t$  with  $S_{t-1}$ . This cell state acts as the memory of the *convlstm* cell, and is passed over to the other cells in the layer for learning useful patterns in the time series. It uses a hyperbolic tangent activation  $\tanh$  instead of sigmoid, and has its own weights and biases  $(w_S, b_S)$  similar to the three gates. These get initialized randomly and are modified based on the loss values and learning over multiple epochs. The final output  $y_t$  for time step  $t$  is computed by convolving the output gate response with activated cell state response  $\tanh(S_t)$ . This continues for the time series over a chosen number of epochs, and the weights and biases are tweaked to optimize the loss function. We use the  $f_1$ -loss as the loss function in this study for training to minimize the false positives and false negatives. Its computation is shown in Equation 4, where TP, FP and FN denote true positives, false positives and false negatives, respectively.

$$fg_t = \sigma_{sm}(w_{fg}[y_{t-1}, x_t] + b_{fg}) \quad \}Forget\ gate \quad 3.1$$

$$\begin{aligned} in_t &= \sigma_{sm}(w_{in}[y_{t-1}, x_t] + b_{in}) \\ \tilde{S}_t &= \tanh(w_S[y_{t-1}, x_t] + b_S) \end{aligned} \quad \}Input\ gate \quad 3.2$$

$$S_t = fg_t * S_{t-1} + in_t * \tilde{S}_t \quad \}Cell\ state \quad 3.3$$

$$\left. \begin{aligned} out_t &= \sigma_{sm}(w_{out}[y_{t-1}, x_t] + b_{out}) \\ y_t &= out_t * \tanh(S_t) \end{aligned} \right\} \text{Output gate}$$

3.3

$$f_1 = 2 \times \left( \frac{\text{precision} \times \text{recall}}{\text{precision} + \text{recall}} \right)$$

$$\text{precision} = \frac{TP}{TP + FP} \quad \text{recall} = \frac{TP}{TP + FN}$$

4

The models in this study are trained using transfer learning. This implies that after running the model on one dataset, the model weights and biases are stored, and these act as initial weights and biases for the next dataset. The configuration of the proposed model is shown in Supplementary Table 2, where *layernorm* and *batchnorm* denote the layer normalization and batch normalization layers (added to avoid overfitting), *relu* denotes the rectified linear unit activation, computed as  $relu(x) = \max(x, 0)$ . The term *dropout* represents the Dropout layer, experimented with different ratios during transfer learning to achieve the best output. Hyperparameters, except for learning and decay rates, are kept the same for learning on different datasets. The hyperparameters used for the urban and coastal model learning are shown in Supplementary Table 3. We trained each dataset with 70% points chosen randomly as training and 30 % as validation. The code and an example data for training the proposed model is available at <https://github.com/ICCT-ML-in-geodesy/InSAR-based-pixel-selection>.

#### 4. Results and Discussion

With multiple urban and coastal datasets trained with two different models, we predicted elite pixels for two urban and two coastal sites, noting the prediction time used per dataset. The prediction outputs for both models are shown in Figure 3, where the left and right columns show pixels selected by the WabInSAR and CLSTM-ISS v2.0 model, respectively. Pixel densities for both urban and coastal datasets are comparable and higher for one coastal (Indian east coast) and one urban dataset (Chicago), as shown in Figure 3I and Supplementary Table 4. The proposed model rejects temporally decorrelated objects like forest trees, water bodies, and snow while selecting man-made objects (buildings and other infrastructure) and agricultural land. The training time varies between 120 to 180 minutes. The prediction time is effectively the time required when the models are deployed to perform elite pixel selection, varying between 3 to 10 minutes as labeled over Figures 3B, D, F and H. We notice that the models outperform all the conventional InSAR processors in terms of computational efficiency, which consumes hours for pixel selection. Further, we achieve this efficiency while using full InSAR image frames and multiple combined frames for training and prediction. We compute the quality of pixel selection using accuracy,

precision, recall and  $f_1$ -score shown in equation 4 using the confusion matrices shown in Supplementary Table 5. The metric outcomes are shown in Figure 3J and also tabulated in Supplementary Table 6. We observe that the prediction accuracy is always above 90 % and reaches 98 % for the Chicago dataset. False positives and false negatives are balanced due to the use of  $f_1$ -loss during model training, and we obtain good  $f_1$ -scores for all the datasets.

Embedding the proposed CLSTM-ISS architecture into the WabInSAR processing chain, we executed the remaining steps, i.e. estimation and removal of nuisance phase components, phase unwrapping and displacement estimation. We perform this to understand the effect of the modified pixel selection over the final InSAR outcome. Figure 4 shows a comparison of the one-dimensional line of sight velocities (1D-LOS) generated from the original WabInSAR processing (first column) and modified WabInSAR processing (second column), replacing the existing pixel selection step with the proposed method for the prediction datasets. As evident from the displacement maps, the velocity maps are similar, and the major deformation zones are seen in both outcomes. We further experimented with test points (random locations) in the test sites and compared the displacement time series. These test points are marked as white pentagons over Figures 4B, D, F, and H. Since the exact location of the test points did not have pixels selected by both methods, we computed the average displacement time series for pixels within 100 meters of the chosen location. Figures 4I, J, K and L show the compared time series for the test points. We see that the pattern is similar, while the magnitudes are slightly varying. We observe that the proposed model retains the quality of time series displacement.

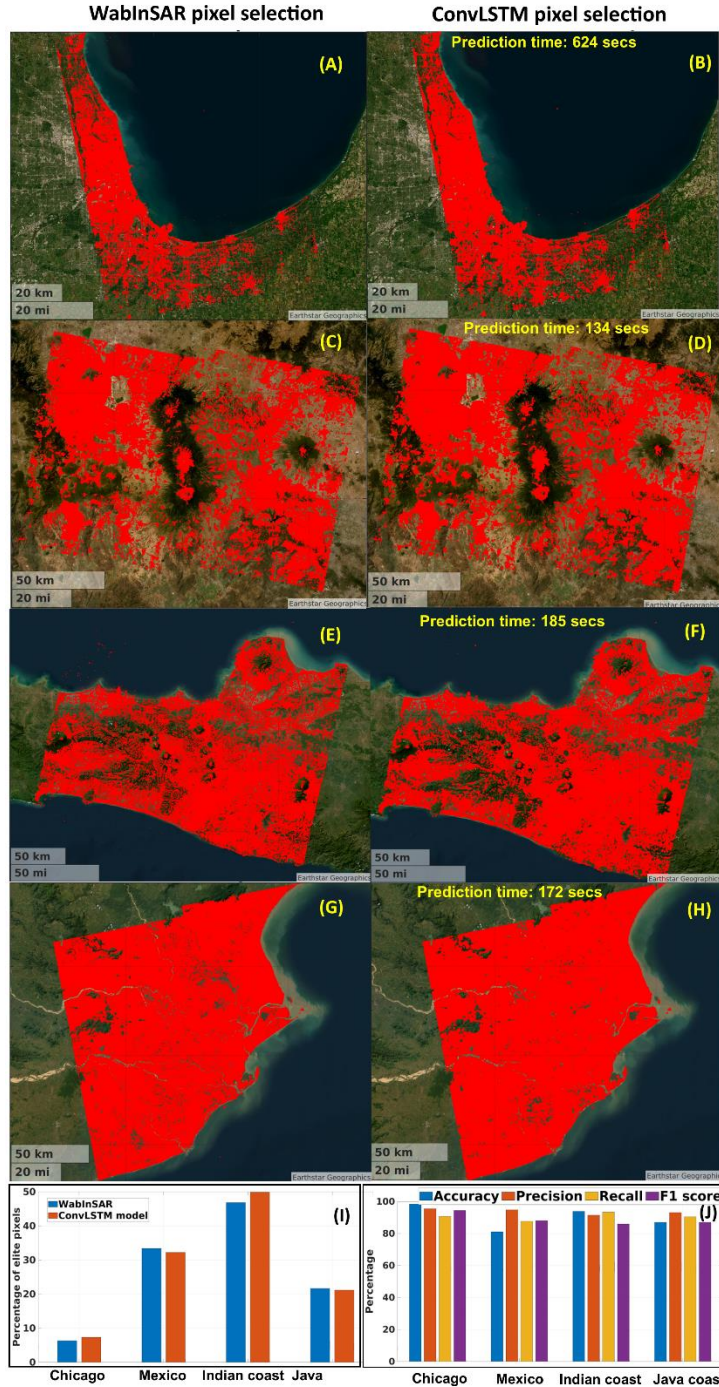


Figure 3: Comparison of pixel selection results from conventional TS-InSAR software (WabInSAR) and the proposed Convolutional LSTM model. The Left and right columns show the results for the predicted urban and coastal sites with WabInSAR and ConvLSTM, respectively. Panels (A), (C), (E) and (G) show WabInSAR-based elite pixel selection for Chicago, Mexico, Java Island and Indian east coast, respectively. Panels (B), (D), (F) and (H) show corresponding CLSTM-ISS model-based selection for Chicago, Mexico, Java Island and Indian east coast, respectively.

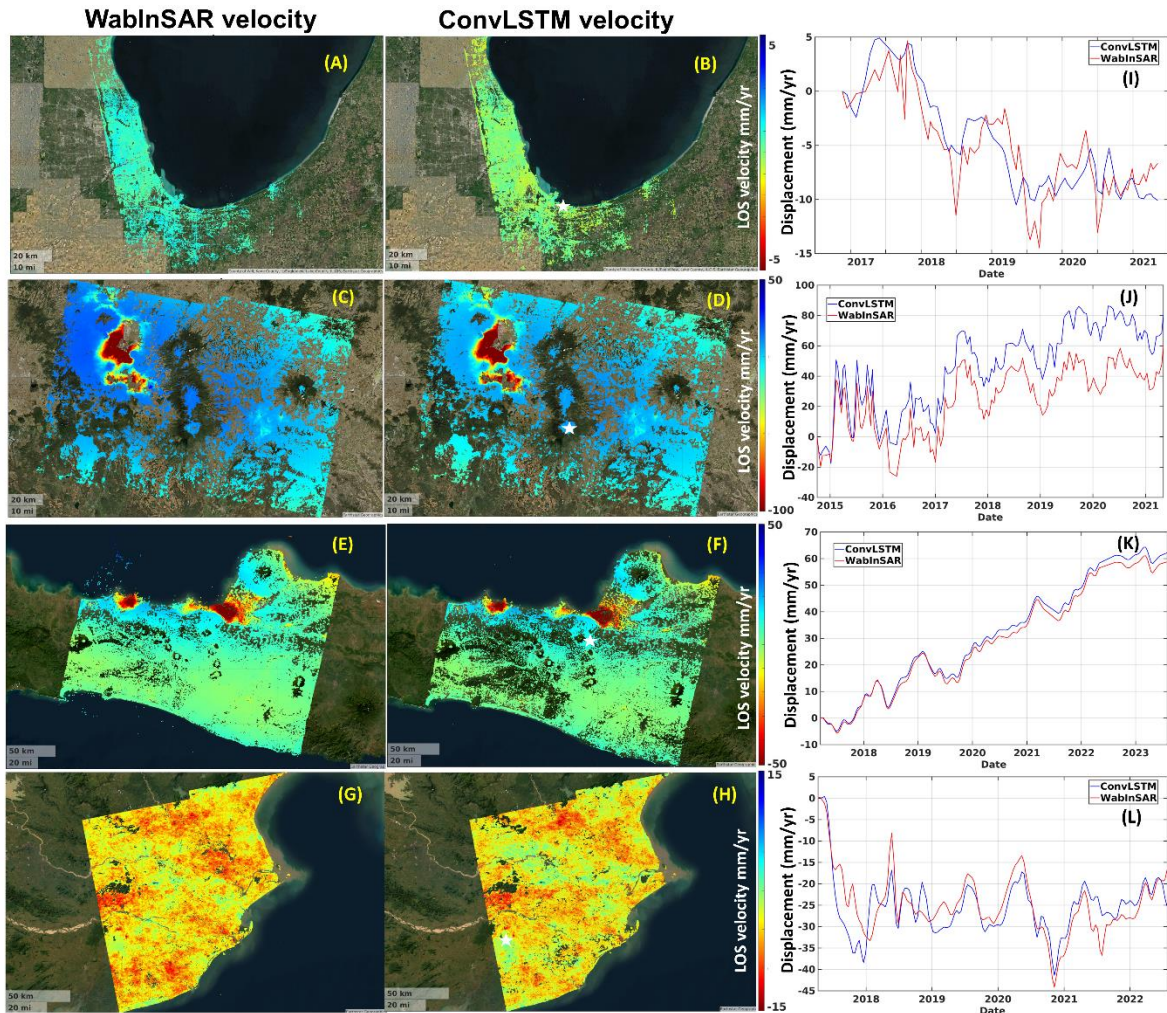


Figure 4: Comparison of displacement maps generated from WabInSAR (first column) and CLSTM-ISS model (second column). Panels (A), (C), (E) and (G) show 1D LOS velocity maps generated from original WabInSAR processing chain for Chicago, Mexico, Java Island and Indian east coast, respectively. Panels (B), (D), (F) and (H) show corresponding velocity maps for Chicago, Mexico, Java Island and Indian east coast, respectively, with modified WabInSAR chain replacing original pixel selection with CLSTM-ISS model-based selection. Colorbars are common for each predicted dataset (e.g. A and B). Panels (I), (J), (K) and (L) show time series comparison plots for test points shown in (B), (D), (F) and (H).

## 5. Conclusion

We propose and demonstrate CLSTM-ISS v2.0, a deep learning-based architecture to speed up and efficiently perform elite pixel selection in time series InSAR. The models trained separately

for urban and coastal sites (also encompassing non-urban terrain) learn from the spatio-temporal behavior of the interferometric phase and efficiently select elite pixels, outperforming the conventional InSAR processors in terms of computational efficiency, generating pixel selection results in order of minutes. The utility of the architecture is demonstrated by embedding it into an existing InSAR processing (WabInSAR) chain, finding that the quality of the final displacement architecture is retained. The architecture can be easily integrated with any InSAR processing chains, promising a quick selection of both PS and DS pixels.

## 6. Acknowledgment

The authors are grateful to the ESA for providing Sentinel-1 IW images. AT and LO are supported by NSF and NASA. MS and NS are supported by DOE.

## 7. Open Research

The code and an example dataset used for training and testing the method developed in this study is available at the following link:

[https://data.lib.vt.edu/articles/dataset/Deep\\_learning\\_for\\_efficient\\_selection\\_of\\_measurement\\_pixels\\_in\\_multi-temporal\\_InSAR\\_processing/23478236](https://data.lib.vt.edu/articles/dataset/Deep_learning_for_efficient_selection_of_measurement_pixels_in_multi-temporal_InSAR_processing/23478236)

## 8. Author contributions

Ashutosh Tiwari: Conceptualization, Methodology, Data curation, Implementation, Validation, Writing – original draft. Nitheshnirmal Sadhasivam: Conceptualization, Methodology, Writing – editing original draft. Leonard O. Ohenhen- Data preparation, Methodology, Writing – editing original draft. Manoochehr Shirzaei: Conceptualization, Methodology, Software, Supervision, Writing – review and editing.

Agram, P., R. Jolivet, B. Riel, Y. Lin, M. Simons, E. Hetland, M. P. Doin, and C. Lasserre (2013), New radar interferometric time series analysis toolbox released, *Eos, Transactions American Geophysical Union*, 94(7), 69-70.

Anantrasirichai, N., J. Biggs, F. Albino, and D. Bull (2019a), A deep learning approach to detecting volcano deformation from satellite imagery using synthetic datasets, *Remote Sensing of Environment*, 230, 111179.

Anantrasirichai, N., J. Biggs, F. Albino, and D. Bull (2019b), The application of convolutional neural networks to detect slow, sustained deformation in InSAR time series, *Geophysical Research Letters*, 46(21), 11850-11858.

Castellazzi, P., N. Arroyo-Domínguez, R. Martel, A. I. Calderhead, J. C. Normand, J. Gárfias, and A. Rivera (2016), Land subsidence in major cities of Central Mexico: Interpreting InSAR-derived land subsidence mapping with hydrogeological data, *International journal of applied earth observation and geoinformation*, 47, 102-111.

Chen, B., J. Yang, Z. Li, C. Yu, Y. Yu, L. Qin, Y. Yang, and H. Yu (2023), A new sequential homogeneous pixel selection algorithm for distributed scatterer InSAR, *GIScience & Remote Sensing*, 60(1), 2218261.

Devara, M., A. Tiwari, and R. Dwivedi (2021), Landslide susceptibility mapping using MT-InSAR and AHP enabled GIS-based multi-criteria decision analysis, *Geomatics, Natural Hazards and Risk*, 12(1), 675-693.

Ferretti, A., A. Fumagalli, F. Novali, C. Prati, F. Rocca, and A. Rucci (2011), A new algorithm for processing interferometric data-stacks: SqueeSAR, *IEEE transactions on geoscience and remote sensing*, 49(9), 3460-3470.

Festa, D., A. Novellino, E. Hussain, L. Bateson, N. Casagli, P. Confuorto, M. Del Soldato, and F. Raspini (2023), Unsupervised detection of InSAR time series patterns based on PCA and K-means clustering, *International Journal of Applied Earth Observation and Geoinformation*, 118, 103276.

Galgani, G., M. Antonelli, M. Bandinelli, E. Scione, and E. Scorzafava (2016), Charging analysis approach on COSMO skymed second generation spacecraft, paper presented at 2016 ESA Workshop on Aerospace EMC (Aerospace EMC), IEEE.

Hajnsek, I., M. Shimada, M. Eineder, K. Papathanassiou, T. Motohka, M. Watanabe, M. Ohki, F. De Zan, P. Lopez-Dekker, and G. Krieger (2014), Tandem-L: Science requirements and mission concept, paper presented at EUSAR 2014; 10th European Conference on Synthetic Aperture Radar, VDE.

Hanssen, R. F. (2001), *Radar interferometry: data interpretation and error analysis*, Springer Science & Business Media.

Hooper, A. (2008), A multi-temporal InSAR method incorporating both persistent scatterer and small baseline approaches, *Geophysical Research Letters*, 35(16).

Hooper, A., P. Segall, and H. Zebker (2007), Persistent scatterer interferometric synthetic aperture radar for crustal deformation analysis, with application to Volcán Alcedo, Galápagos, *Journal of Geophysical Research: Solid Earth*, 112(B7).

Jiang, M., X. Ding, R. F. Hanssen, R. Malhotra, and L. Chang (2014), Fast statistically homogeneous pixel selection for covariance matrix estimation for multitemporal InSAR, *IEEE transactions on geoscience and remote sensing*, 53(3), 1213-1224.

Kellogg, K., P. Hoffman, S. Standley, S. Shaffer, P. Rosen, W. Edelstein, C. Dunn, C. Baker, P. Barela, and Y. Shen (2020), NASA-ISRO synthetic aperture radar (NISAR) mission, paper presented at 2020 IEEE Aerospace Conference, IEEE.

Lattari, F., A. Rucci, and M. Matteucci (2022), A deep learning approach for change points detection in InSAR time series, *IEEE Transactions on Geoscience and Remote Sensing*, 60, 1-16.

Lee, J.-C., and M. Shirzaei (2023), Novel algorithms for pair and pixel selection and atmospheric error correction in multitemporal InSAR, *Remote Sensing of Environment*, 286, 113447.

Mari, S., G. Valentini, S. Serva, T. Scopa, M. Cardone, L. Fasano, and G. F. De Luca (2018), COSMO-SkyMed second generation system access portfolio, *IEEE Geoscience and Remote Sensing Magazine*, 6(1), 35-43.

Moreira, A., G. Krieger, M. Younis, I. Hajnsek, K. Papathanassiou, M. Eineder, and F. De Zan (2011), Tandem-L: A mission proposal for monitoring dynamic earth processes, paper presented at 2011 IEEE International Geoscience and Remote Sensing Symposium, IEEE.

Ohenhen, L. O., M. Shirzaei, and P. L. Barnard (2024), Slowly but surely: Exposure of communities and infrastructure to subsidence on the US east coast, *PNAS nexus*, 3(1), pgad426.

Ohenhen, L. O., M. Shirzaei, C. Ojha, and M. L. Kirwan (2023), Hidden vulnerability of US Atlantic coast to sea-level rise due to vertical land motion, *Nature Communications*, 14(1), 2038.

Parsons, T., P. C. Wu, M. Wei, and S. D'Hondt (2023), The Weight of New York City: Possible Contributions to Subsidence From Anthropogenic Sources, *Earth's Future*, 11(5), e2022EF003465.

Qiao, X., T. Chu, and P. Tissot (2023a), Coastal Subsidence Analysis Between Houston and Galveston, Texas, USA, paper presented at IGARSS 2023-2023 IEEE International Geoscience and Remote Sensing Symposium, IEEE.

Qiao, X., T. Chu, P. Tissot, and S. Holland (2023b), Sentinel-1 InSAR-derived land subsidence assessment along the Texas Gulf Coast, *International Journal of Applied Earth Observation and Geoinformation*, 125, 103544.

Qu, F., Z. Lu, J. Kim, and M. J. Turco (2023), Mapping and characterizing land deformation during 2007–2011 over the Gulf Coast by L-band InSAR, *Remote Sensing of Environment*, 284, 113342.

Radman, A., M. Akhoondzadeh, and B. Hosseiny (2021), Integrating InSAR and deep-learning for modeling and predicting subsidence over the adjacent area of Lake Urmia, Iran, *GIScience & Remote Sensing*, 58(8), 1413-1433.

Reza, T., A. Zimmer, J. M. D. Blasco, P. Ghuman, T. K. Aasawat, and M. Ripeanu (2017), Accelerating persistent scatterer pixel selection for InSAR processing, *IEEE Transactions on Parallel and Distributed Systems*, 29(1), 16-30.

Rosen, P. A., and R. Kumar (2021), NASA-ISRO SAR (NISAR) Mission Status, paper presented at 2021 IEEE Radar Conference (RadarConf21), IEEE.

Rosenqvist, A., et al. (2023), A Combined CEOS-ARD Format Specification for Synthetic Aperture Radar, in *CEOS WGCV SAR Workshop*, edited, Oberpfaffenhofen, Germany.

Rouet-Leduc, B., R. Jolivet, M. Dalaison, P. A. Johnson, and C. Hulbert (2021), Autonomous extraction of millimeter-scale deformation in InSAR time series using deep learning, *Nature communications*, 12(1), 6480.

Rygu, M., A. Novellino, E. Hussain, F. Syafiudin, H. Andreas, and C. Meisina (2023), A clustering approach for the analysis of InSAR Time Series: Application to the Bandung Basin (Indonesia), *Remote Sensing*, 15(15), 3776.

Sherpa, S. F., M. Shirzaei, and C. Ojha (2023), Disruptive Role of Vertical Land Motion in Future Assessments of Climate Change-Driven Sea Level Rise and Coastal Flooding Hazards in the Chesapeake Bay, *Journal of Geophysical Research: Solid Earth*, e2022JB025993.

Shirzaei, M. (2012), A wavelet-based multitemporal DInSAR algorithm for monitoring ground surface motion, *IEEE Geoscience and Remote Sensing Letters*, 10(3), 456-460.

Sica, F., F. Calvanese, G. Scarpa, and P. Rizzoli (2020), A CNN-based coherence-driven approach for InSAR phase unwrapping, *IEEE Geoscience and Remote Sensing Letters*, 19, 1-5.

Tiwari, A., and M. Shirzaei (2024), A novel machine learning and deep learning semi-supervised approach for automatic detection of InSAR-based deformation hotspots, *International Journal of Applied Earth Observation and Geoinformation*, 126, 103611.

Tiwari, A., A. B. Narayan, and O. Dikshit (2020), Deep learning networks for selection of measurement pixels in multi-temporal SAR interferometric processing, *ISPRS Journal of Photogrammetry and Remote Sensing*, 166, 169-182.

Wang, C., X.-S. Wang, Y. Xu, B. Zhang, M. Jiang, S. Xiong, Q. Zhang, W. Li, and Q. Li (2022), A new likelihood function for consistent phase series estimation in distributed scatterer interferometry, *IEEE Transactions on Geoscience and Remote Sensing*, 60, 1-14.

Wu, P. C., M. Wei, and S. D'Hondt (2022), Subsidence in coastal cities throughout the world observed by InSAR, *Geophysical Research Letters*, 49(7), e2022GL098477.

Xi, D., N. Lin, and A. Gori (2023), Increasing sequential tropical cyclone hazards along the US East and Gulf coasts, *Nature Climate Change*, 13(3), 258-265.

Yin, J. (2023), Rapid Decadal Acceleration of Sea Level Rise along the US East and Gulf Coasts during 2010–22 and Its Impact on Hurricane-Induced Storm Surge, *Journal of Climate*, 36(13), 4511-4529.

Yuan, R., and J. Chen (2022), A hybrid deep learning method for landslide susceptibility analysis with the application of InSAR data, *Natural Hazards*, 114(2), 1393-1426.

Zhang, Z., Q. Zeng, and J. Jiao (2022), Deformations monitoring in complicated-surface areas by adaptive distributed Scatterer InSAR combined with land cover: Taking the Jiaju landslide in Danba, China as an example, *ISPRS Journal of Photogrammetry and Remote Sensing*, 186, 102-122.

Zhou, L., H. Yu, V. Pascazio, and M. Xing (2022), PU-GAN: a one-step 2-D InSAR phase unwrapping based on conditional generative adversarial network, *IEEE Transactions on Geoscience and Remote Sensing*, 60, 1-10.

## Supporting Information for

### Leveraging power of deep learning for fast and efficient elite pixel selection in time series interferometry

Ashutosh Tiwari\*, Nitheshnirmal Sadhashivam, Leonard O. Ohenhen and Manoochehr Shirzaei  
Department of Geosciences, Virginia Tech, Blacksburg, VA, USA  
Virginia Tech National Security Institute, Blacksburg, VA, USA

#### Contents of this file

Tables 1 to 5.

#### Introduction

We provide supporting information to the main text related to the datasets used for training the proposed deep learning architecture, its configuration and training parameters. We also add a few tables related to interpretation of the results obtained from the proposed architecture.

Table 1.1. Urban datasets used for training and testing.

Type	Dataset	Path	Frame(s)	Orbit	No. of Images	Temporal coverage	Training/Prediction time (mins)
Training (Urban)	LA	64	108	ASC	79	2015-2021	124
	NY	33	130	ASC	81	2017-2021	121
	Phoenix	20	103, 108	ASC	79	2014-2021	134
	Houston	34	90, 95	ASC	82	2016-2021	138
Testing (Urban)	Chicago	121	130,135	ASC	80	2016-2021	10.5 (prediction)
	Mexico City	143	526, 531	DES	137	2014-2021	2.5 (prediction)

Table 1.2. Coastal datasets used for training and testing.

Type	Dataset	Path	Frame(s)	Orbit	No. of Images	Temporal coverage	Training/Prediction time (mins)
------	---------	------	----------	-------	---------------	-------------------	---------------------------------

Training (Coastal)	Chesapeake Bay	4	115	ASC	116	2016-2020	124
	Miami, Port St. Lucie	48	79, 84	ASC	101	2015-2020	121
	Boston, Yarmouth	62	133	ASC	116	2016-2020	134
	Southport, Wilmington	77	107	ASC	112	2017-2020	138
	Rhode Island, Brookhaven	135	131	ASC	115	2016-2020	136
	Savannah, Richmond Hill	150	102	ASC	124	2015-2020	132
Testing (Coastal)	Indian East Coast	65	83	ASC	156	2017-2022	3 (prediction)
	Java Island coast	76	613, 618	DES	167	2017-2023	3 (prediction)

Table 2. CLSTM-ISS v2.0 network configuration. Total trainable and non-trainable parameters are 93281 and 32 respectively. The terms  $n_s$  and  $n_t$  represent the number of image samples and time steps respectively.

Layer (type)	Parameters	Output dimension
$(convlstm_1) + layernorm + relu$	No. of filters: 16	$(n_s, n_t, 100, 100, 16)$
$(convlstm_2) + batchnorm + relu$	No. of filters: 16	$(n_s, n_t, 100, 100, 16)$
$(conv+BN)2+relu$	No. of filters: 16	$(n_s, 100, 100, 16)$
$dropout$	Ratio: (0.2, 0.25, 0.3)	$(n_s, 100, 100, 16)$
$FC$		$(n_s, 100, 100, 1)$

Table 3. Hyperparameters used for training the proposed models.

Hyper-parameter	Values
Loss function	$f_l$ loss
Performance metric	$f_l$ score, accuracy, precision, recall
Training epochs	20 to 200 epochs per dataset
Early stopping criteria	5 epochs
Optimizer	Adam
Learning rate	(0.01, 0.001)
Decay rate	$(10^{-5}, 10^{-4})$

Table 4. Comparison of pixel densities generated from WabInSAR and CLSTM-ISS model.

S.No.	Site	WabInSAR pixel density	CLSTM-ISS pixel density	Prediction time by CLSTM-ISS (seconds)
1	Chicago	6.32	7.31	624
2	Mexico	33.40	32.23	134
3	Indian East Coast	46.82	49.88	185

4	Java Island coast	21.66	21.16	172
---	-------------------	-------	-------	-----

Table 5. Confusion matrices for test sites.

Chicago	Predicted	Actual	
		Positive	Negative
	Positive	13913433 (TP)	208560 (FP)
Negative	58896 (FN)	893961 (TN)	

Mexico	Predicted	Actual	
		Positive	Negative
	Positive	1401500 (TP)	36240 (FP)
Negative	61475 (FN)	659709 (TN)	

Indian coast	Predicted	Actual	
		Positive	Negative
	Positive	1268420 (TP)	166269 (FP)
Negative	83776 (FN)	1179527 (TN)	

Java coast	Predicted	Actual	
		Positive	Negative
	Positive	4585244 (TP)	153773 (FP)
Negative	183806 (FN)	1126922 (TN)	

Table 6. Prediction scores for the proposed CLSTM-ISS model.

S.No	Metric	Chicago	Mexico	Indian East Coast	Java Coast
1	Accuracy	98.22	95.47	90.73	94.41
2	Precision	81.08	94.79	87.64	87.99
3	Recall	93.81	91.47	93.36	85.97
4	F1-score	86.98	93.10	90.41	86.97